



## An ice-sheet wide framework for englacial attenuation and basal reflection from ice penetrating radar data

T. M. Jordan<sup>1</sup>, J. L. Bamber<sup>1</sup>, C. N. Williams<sup>1</sup>, J. D. Paden<sup>2</sup>, M. J. Siegert<sup>3</sup>,  
P. Huybrechts<sup>4</sup>, O. Gagliardini<sup>5</sup>, and F. Gillet-Chaulet<sup>6</sup>

<sup>1</sup>Bristol Glaciology Centre, School of Geographical Sciences, University of Bristol, Bristol, UK.

<sup>2</sup>Center for Remote Sensing of Ice-Sheets, University of Kansas, Lawrence, USA.

<sup>3</sup>Grantham Institute and Earth Science and Engineering, Imperial College, University of London, London, UK.

<sup>4</sup>Department of Geography, Vrije Universiteit Brussels, Brussels, Belgium.

<sup>5</sup>Le Laboratoire de Glaciologie et Géophysique de l'Environnement, University Grenoble Alpes, Grenoble, France.

<sup>6</sup>Le Laboratoire de Glaciologie et Géophysique de l'Environnement, Centre National de la Recherche Scientifique, Grenoble, France.

*Correspondence to:* T. M. Jordan (tom.jordan@bris.ac.uk) or J. L. Bamber (j.bamber@bris.ac.uk)

**Abstract.** Radar-inference of the bulk properties of glacier beds, most notably identifying basal melting, is, in general, derived from the basal reflection coefficient. On the scale of an ice-sheet, unambiguous determination of basal reflection is primarily limited by uncertainty in the englacial attenuation of the radio wave, which is an exponential function of temperature. Most existing radar algorithms assume stationarity in the attenuation rate, which is not feasible at an ice-sheet wide scale. Here we introduce a new framework for deriving englacial attenuation and basal reflection, and, to demonstrate its efficacy, we apply it to the Greenland Ice-Sheet. A central feature is the use of a prior Arrhenius temperature model to estimate the spatial variation in englacial attenuation as a first guess input for the radar algorithm. We demonstrate regions of solution convergence for two input temperature fields, and for independently analysed field campaigns. The coverage achieved is a trade-off with uncertainty and we propose that the algorithm can be ‘tuned’ for discrimination of basal melt (attenuation loss uncertainty  $\sim 5$  dB). This is supported by our physically realistic ( $\sim 20$  dB) range for the basal reflection coefficient. Finally, we show that the attenuation solution can be used to predict the temperature bias of thermomechanical ice-sheet models.

### 15 1 Introduction

Ice Penetrating Radar (IPR) data provide valuable insights into several physical properties of glaciers and their beds including: ice thickness (e.g. Fretwell et al. (2013); Bamber et al. (2013)), bed roughness (e.g. Berry (1973); Siegert et al. (2005); Rippin (2013)), basal material properties (e.g. Oswald and Gogineni (2008); Jacobel et al. (2009); Fujita et al. (2012); Schroeder et al. (2016)), internal layer structure (e.g. Matsuoka et al. (2010); Macgregor et al. (2015a)), and englacial temperature



(Macgregor et al., 2015b). In recent years, there has been a noticeable increase in radar track density in Greenland and parts of Antarctica, which has led to the development of new ice-sheet wide data products for bed elevation and ice thickness (Fretwell et al., 2013; Bamber et al., 2013). These data products provide essential boundary conditions for numerical models of ice-sheets (e.g. Gillet-Chaulet et al. (2012); Cornford et al. (2015)), and enable investigation of a diversity of topics related to ice-sheet dynamics. By contrast, despite many notable regional studies (e.g. Oswald and Gogineni (2008); Jacobel et al. (2009); Fujita et al. (2012); Schroeder et al. (2016)), ice-sheet wide data products for bulk basal material properties, such as quantifying regions of basal melt, do not yet exist. As contemporary models of ice-sheet dynamics have been demonstrated to be highly sensitive to basal traction (Price et al., 2011; Nowicki et al., 2013; Ritz et al., 2015), the poorly constrained basal interface poses a problem for their predictive accuracy.

Bulk material properties of glacier beds can, in principle, be identified from their basal (radar) reflection coefficient (Bogorodsky et al., 1983a; Peters, 2005; Oswald and Gogineni, 2008). The basal reflection coefficient is predicted to vary over a  $\sim 20$  dB range for different sub-glacial materials, with water having a  $\sim 10$  dB higher value than the most reflective frozen bed rock (Bogorodsky et al., 1983a). On an ice-sheet wide scale, unambiguous radar-inference of basal melt from bed reflections is limited primarily by uncertainty in the spatial variation of englacial attenuation (MacGregor et al., 2012; Matsuoka, 2011). Arrhenius models, where the attenuation rate is an exponential function of temperature (Corr et al., 1993; MacGregor et al., 2007; Macgregor et al., 2015a), predict that the depth-averaged attenuation rate varies by a factor of  $\sim 8$  over the scale of the Antarctic Ice-Sheet (Matsuoka et al., 2012a). These models are, however, strongly limited by both inherent uncertainty in model parameters ( $\sim 20$ -25% fractional error) (MacGregor et al., 2007, 2012; Macgregor et al., 2015a), and high sensitivity to the input temperature field, which itself is poorly constrained. Despite this evidence for spatial variation in attenuation, the majority of radar-algorithms for the inference of attenuation and basal reflection make the implicit assumption that the attenuation rate is locally stationary e.g. Gades et al. (2000); Winebrenner et al. (2003); Jacobel et al. (2009); Fujita et al. (2012). These radar algorithms, which use the relationship between bed-returned power and ice thickness to identify an attenuation trend, are suspected to yield erroneous values (Matsuoka, 2011; Schroeder et al., 2016). Moreover, these radar algorithms are not tuned for automated application over the scale of an ice-sheet.

In this study we introduce a new ice-sheet wide framework for the radar-inference of attenuation and basal reflection and apply it to IPR data from the Greenland Ice-sheet (GrIS). A central feature of our algorithm is the use of a prior Arrhenius model estimation of the attenuation rate as an initial condition. Conceptually, the initial condition is used to estimate regions where the assumption of stationarity is valid within some specified tolerance. Specifically, the estimate is used to: (i) constrain a moving window for the algorithm sample region, (ii) to standardise the power for local variation in attenuation within each sample region, (iii) to implement algorithm quality control. We demonstrate



regions of algorithm solution convergence for two different input temperature fields and for inde-  
pendently analysed IPR data. The coverage provided by the algorithm is a trade-off with solution  
60 accuracy, and we suggest that the algorithm can be ‘tuned’ for basal melt discrimination in restricted  
regions of the GrIS. This is supported by the decibel range for the basal reflection coefficients ( $\sim$   
20 dB on the scale of a major drainage basin). Additionally, we show that the attenuation rate solu-  
tion can be used to infer bias in the depth-averaged temperature field of thermomechanical ice-sheet  
models.

## 65 2 Data and methods

### 2.1 Ice penetrating radar data

The airborne IPR data used in this study were collected by the Center for Remote Sensing of Ice  
Sheets (CReSIS) within the Operation IceBridge project. Four field seasons from 2011-2014 (months  
March-May) have been analysed in this proof of concept study. These field seasons are the most spa-  
70 tially comprehensive to date, with coverage throughout all the major drainage basins of the GrIS  
and relatively dense across-track spacing toward the ice margins (Fig. 1). The radar instrument, the  
Multi-Channel Coherent Radar Depth Sounder (MCoRDS), has been installed on a variety of plat-  
forms and has a programmable frequency range. However, for the data used in this study, it is always  
operated on the NASA P-3B Orion aircraft and uses a frequency range from 180 MHz to 210 MHz,  
75 which, after accounting for pulse shaping and windowing, corresponds to a depth-range resolution  
in ice of 4.3 m (Rodriguez-Morales et al., 2014; Paden, 2015). The data processing steps to produce  
the multi-looked Synthetic Aperture Radar (SAR) images used in this work, are described in Gogi-  
neni et al. (2014). The along-track resolution after SAR processing and multilooking depends on the  
season and is either  $\sim 30$  m or  $\sim 60$  m with a sample spacing of  $\sim 15$  m or  $\sim 30$  m respectively.  
80 The radar’s dynamic range is controlled using a waveform playlist which allows low and high gain  
channels to be multiplexed in time. The digitally recorded gain for each channel allows radiomet-  
ric calibration and, in principle, enables power measurements from different flight tracks and field  
seasons to be combined. This is in contrast to pre 2003 CReSIS Greenland datasets, which used a  
manual gain control that was not recorded in the data stream.

### 85 2.2 Overview of algorithm

A flow diagram for the separate components of the radar algorithm is shown in Fig. 2. The along-  
track processing of the IPR data (Sect. 2.3) is an adaptation of the method developed by Oswald  
and Gogineni (2008, 2012), and is particularly suited to evaluation of bulk material properties  
via the reflection coefficient. The Arrhenius model estimation of the attenuation rate, (Sect. 2.4),  
90 uses the framework developed by MacGregor et al. (2007); Macgregor et al. (2015b) and assumes  
steady-state temperature fields from the GISM (Greenland Ice-Sheet Model) (Huybrechts, 1996),



and SICOPOLIS (Simulation COde for POLythermal Ice-Sheets) (Greve, 1997) thermomechanical models. The Arrhenius model is used to firstly constrain the sample region for the algorithm (Sect. 2.5), and then to correct for local attenuation variation within each region when inferring the attenuation rate, (Sect. 2.6). Algorithm quality control is then implemented, by testing for regions where the attenuation solution is marked by strong correlation between bed-returned power and ice thickness, (Sect. 2.7). Finally, gridded maps are produced for the radar-inferred attenuation rate, the total attenuation loss, and the basal reflection coefficient, (Sect. 2.8).

### 2.3 Waveform processing

The processing of the IPR data, based upon the method developed by Oswald and Gogineni (2008, 2012), uses an along-track (phase-incoherent) average of the basal waveform and a depth aggregated/integrated definition of the bed-returned power. The advantage of using this definition, compared with the conventional peak power definition, is that the variance due to variable surface roughness (e.g. Berry (1973); Peters (2005)) is reduced. This reduction in variance is thought to occur because, based on conservation of energy principles, the aggregated definition of bed-returned power for a diffuse surface is more directly related to the predicted (specular) reflection coefficients than equivalent peak power values (Oswald and Gogineni, 2008). In our study we make two important modifications to this method, which are described here, along with an overview of the key processing steps. The first modification corresponds to defining a variable window size for the along-track averaging of the basal waveform (which enables us to optimise the effective data resolution in thin ice), and the second corresponds to the implementation of an automated waveform quality control procedure.

Using the waveform processing method of Oswald and Gogineni (2008, 2012), the along-track waveform averaging window is set using the first return radius

$$r = \sqrt{p \left( s + \frac{h}{\sqrt{\epsilon_{ice}}} \right)}, \quad (1)$$

where  $p=4.99$  m is the (pre-windowed) radar pulse half-width in air (Rodriguez-Morales et al., 2014),  $s$  is the height of the radar sounder above the ice surface,  $h$  is the ice thickness and,  $\epsilon_{ice} = 3.15$  is the real part of the relative dielectric permittivity for ice. For a flat surface,  $r$ , corresponds to the radius of the circular region illuminated by the radar pulse such that it extends the initial echo return by <50% (Oswald and Gogineni, 2008). Additionally, if adjacent waveforms within this region are stacked about their initial returns and arithmetically averaged, they represent a phase-incoherent average where the effects of power fluctuations due to interference are smoothed (Oswald and Gogineni, 2008; Peters, 2005). Oswald and Gogineni (2008, 2012) considered the northern interior of the GrIS where  $h \sim 3000$  m, and subsequently  $r$  and the along-track averaging interval were approximated as being constant. Since our study considers IPR data from both the ice margins and interior, we use Eq. (1) to define a variable size along-track averaging window. For the typical flying height of



$s=480$  m,  $r$  ranges from  $\sim 55$  m in thin ice ( $h=200$  m) to  $\sim 105$  m in thick ice ( $h=3000$  m), though can be higher during plane maneuvers. The number of waveforms in each averaging window is then obtained by dividing  $2r$  by the along-track resolution.

130 The incoherently averaged basal waveforms range from sharp pulse-like returns associated with specular reflection, to broader peaks associated with diffuse reflection (refer to Oswald and Gogineni (2008) for a full discussion). An example of an incoherently averaged waveform is shown in Fig. 3a, in units of linear power versus depth-range index  $D_i$ . The plot shows the upper and lower limits of the power depth integral,  $D_{lower}$  and  $D_{upper}$ . These limits are symmetric about the peak power  
 135 value, with  $(D_{upper} - D_{lower}) = 2r$  (in units of the depth-range index), a range motivated by the observed fading intervals described in (Oswald and Gogineni, 2008). Subsequently, as is the case for the along-track averaging bin, the power integral limits vary over the extent of the ice-sheet and are of greater range in thicker ice. The aggregated (integrated) power is then defined by

$$P_{agg} = \sum_{D_i=D_{lower}}^{D_i=D_{upper}} P(D_i). \quad (2)$$

140 Waveform quality control, was implemented by testing if the waveform decays to a specified fraction of the peak power value within the integral limits  $D_{lower}$  and  $D_{upper}$ . This effectively provides a test that the SAR beamwidth is large enough to include all of the scattered energy, which was argued to be the general case by Oswald and Gogineni (2008). Decay fractions of 1%, 2% and 5% were considered, and 2% was established to give the best coverage, whilst excluding obvious waveform  
 145 anomalies. The waveform in Fig. 3a is an example that satisfies the quality control measure, whereas the waveform shown in Fig. 3b does not. The relative decibel power for each waveform is then defined by

$$[P] = 10 \log_{10} (P_{agg}), \quad (3)$$

where the decibel notation  $[X] = 10 \log_{10} X$  is used. Finally, the relative power is corrected for the  
 150 effects of geometrical spreading using

$$[P^C] = [P] - [G], \quad (4)$$

where

$$[G] = 20 \log_{10} \frac{g \lambda_0}{8\pi \left( s + \frac{h}{\sqrt{\epsilon_{ice}}} \right)}, \quad (5)$$

(Bogorodsky et al., 1983b) with  $g = 4$  the antenna gain (corresponding to 11.8 dBi) (Paden, 2015),  
 155 and  $\lambda_0=1.54$  m the central wavelength of the radar pulse (Rodriguez-Morales et al., 2014).

#### 2.4 Arrhenius temperature model for attenuation

It is well established that the radar attenuation rate in glacier ice is described by an Arrhenius relationship where there is exponential dependence upon temperature and a linear dependence upon



the concentration of soluble ionic impurities (Corr et al., 1993; MacGregor et al., 2007; Macgregor  
160 et al., 2015a; Stillman et al., 2013). The Arrhenius relationship is empirical and the dielectric prop-  
erties of impure glacier ice, (pure ice conductivity, molar conductivities of soluble ionic impurities,  
and activation energies), need to be measured with respect to a reference temperature. An Arrhe-  
nius modelling framework has recently been developed for the GrIS, from herein referred to as the  
M07 model following MacGregor et al. (2007); Macgregor et al. (2015a), that includes three sol-  
165 ule ionic impurities: hydrogen/acidity ( $H^+$ ), chlorine/sea salt ( $Cl^-$ ), and ammonium ( $NH_4^+$ ). The  
equations and parameters for the M07 model calculation of the attenuation rate,  $B_\infty$  (in  $dB\ km^{-1}$ ),  
the depth-averaged attenuation rate  $\langle B_\infty \rangle$ , (in  $dB\ km^{-1}$ ), and the total loss  $[L_\infty]$  (in dB) are out-  
lined in Appendix A. The  $\infty$  subscript is used for these quantities as they are derived from the high  
170 frequency limit of the electrical conductivity,  $\sigma_\infty$ , and it enables them to be distinguished from the  
corresponding radar-inferred values, (introduced in Sect. 2.6), which have no subscript. For brevity,  
in the rest of the paper we refer to the depth-averaged attenuation rate,  $\langle B_\infty \rangle$ , as the attenuation  
rate.

The Arrhenius model assumes uniform, depth-averaged, molar concentrations:  $c_{H^+}=0.8\ \mu M$ ,  $c_{Cl^-}=1.0$   
 $\mu M$  and  $c_{NH_4^+}=0.4\ \mu M$ , which are derived from GRIP core data (Macgregor et al., 2015b). A decom-  
175 position of the temperature dependence for  $B_\infty$  for pure ice and the different ionic species is shown  
in Fig. 4a. The pure ice component dominates at higher temperatures, (for example at  $-10^\circ C \sim 84\%$   
of the total attenuation rate is due to the pure ice component), whilst the  $H^+$  component is signif-  
icantly greater than the  $Cl^-$  and  $NH_4^+$  components at all temperatures. Use of layer stratigraphy  
for the concentration of the ionic species (rather than depth-averaged values) is discussed in detail  
180 in MacGregor et al. (2012), and is considered less crucial for an attenuation model than spatially  
varying temperature.

The prior estimation of  $\langle B_\infty \rangle$  and  $[L_\infty]$  was obtained using the steady state temperature fields  
for GISM and SICOPOLIS and is explained fully in Appendix A. The calculation was interpolated  
at 1 km grid resolution, and used the Greenland Bedmap 2013 thickness data product (Bamber et al.,  
185 2013). For the SICOPOLIS temperature field it is necessary to convert the (homologous) temperature  
values from degrees below pressure melting point to units of K (or  $^\circ C$ ) using a depth correction factor  
of  $-8.7 \times 10^{-4}\ K\ m^{-1}$  (Price et al., 2015). For both temperature fields, the depth-averaged attenuation  
rate is predicted to vary extensively over the GrIS, with minimum values in the interior  $\sim 7\ dB\ km^{-1}$   
and maximum values for the south western margins of  $> 35\ dB\ km^{-1}$  (shown for the GISM field in  
190 Fig. 4b). For the majority of the IPR data coverage region GISM has a negative temperature bias,  
and therefore depth-averaged attenuation rate bias, with respect to SICOPOLIS (Fig. 4c). The GISM  
vertical temperature profiles are in better overall agreement with the temperature profiles at the deep  
ice core sites shown in Fig. 1b (refer to Macgregor et al. (2015b) for summary plots of the core  
temperature profiles).



## 195 2.5 Constraining the algorithm sample region

Radar-inference of the depth-averaged attenuation rate requires sampling IPR data from a local re-  
 gion of the ice-sheet with a range of ice thicknesses (Gades et al., 2000; MacGregor et al., 2007;  
 Jacobel et al., 2009; Fujita et al., 2012; Matsuoka et al., 2012b). An implicit assumption of the  
 method, which considers the relationship between bed-returned power and ice thickness, is that the  
 200 depth-averaged attenuation rate is stationary across the sample region (Matsuoka et al., 2010; Lay-  
 berry and Bamber, 2001). However, as was shown in Sect. 2.4, the depth-averaged attenuation rate  
 is predicted to have pronounced spatial variation, and therefore an ice-sheet wide radar attenuation  
 algorithm must take this into account. In our development of an automated framework, we use the  
 spatial distribution of  $\langle B_\infty \rangle$  (the prior Arrhenius model estimate) firstly to constrain the size and  
 205 shape of the sample region (described here), and secondly to correct for local attenuation variation  
 within each sample region (described in Sect. 2.6). The steps for determining the sample region ‘tar-  
 get window’ size as a function of position (assuming a 1 km scan resolution) are described below.

Fig.5a illustrates an example of the anisotropy that can occur in the spatial distribution of  $\langle B_\infty \rangle$   
 for a 120 km<sup>2</sup> region of the GrIS. For simplicity of computational implementation the target win-  
 210 dows is divided into eight segments, (notated by  $S_n$  with  $n=1,2,\dots,8$ ), in a plane-polar coordinate  
 system about a central point  $(x_0, y_0)$ , (Fig. 5b). The size of each segment is defined by its cen-  
 tral radius vector,  $R_n$ , for angles  $\theta_n = \frac{(n-1)\pi}{8}$ .  $\langle B_\infty \rangle$  is then approximated in the plane-polar  
 coordinate system by defining the attenuation rate in each segment to have the same radial de-  
 pendence as along the direction of the central radius vector:  $\langle B_\infty(r) \rangle = \langle B_\infty(r_n, \theta_n) \rangle$  with  
 215  $r = \sqrt{(x - x_0)^2 + (y - y_0)^2}$  (Fig. 5c). The Euclidean distance of  $\langle B_\infty \rangle$  from  $(x_0, y_0)$  is then  
 used to define a tolerance metric, shown for  $\sqrt{(\langle B_\infty(x, y) \rangle - \langle B_\infty(x_0, y_0) \rangle)^2}$  in Fig. 5d and  
 the segment approximation  $\sqrt{(\langle B_\infty(r_n, \theta_n) \rangle - \langle B_\infty(x_0, y_0) \rangle)^2}$  in Fig. 5e respectively.

A primary consideration for the spatially varying moving target window is that the target window  
 dimensions,  $R_n$ , are smoothly varying in space. If the converse were true then there would be a sharp  
 220 discontinuity in the IPR data that is sampled. It was established that, rather than use of a simple  
 maximum Euclidean distance criteria to define  $R_n$ , a Root Mean Square (RMS) integral measure  
 produces greater spatial continuity. The RMS measure, which is similar to the RMS integral measure  
 for a continuous-time function, is defined for each segment by

$$RMS(R_n) = \sqrt{\int_0^{R_n} \frac{\pi}{4} (\langle B_\infty(r_n, \theta_n) \rangle - \langle B_\infty(x_0, y_0) \rangle)^2 r_n dr_n \frac{\pi R_n^2}{8}}. \quad (6)$$

225 Specifying a value of  $RMS(R_n)$ , then enables radius vectors  $R_n$  to be derived from evaluating  
 the integral, Eq. (6). It was further established that smoother windowing occurs if the constraints



$$\begin{aligned}
 R_1 = R_5, R_2 = R_6, R_3 = R_7, R_4 = R_8, \text{ are applied and the joint integral} \\
 RMS(R_n) = \frac{1}{2} \sqrt{\int_0^{R_n} \frac{\pi}{4} (\langle B_\infty(r_n, \theta_n) \rangle - \langle B_\infty(x_0, y_0) \rangle)^2 r_n dr_n} \\
 + \frac{1}{2} \sqrt{\int_0^{R_n} \frac{\pi}{4} (\langle B_\infty(r_m, \theta_m) \rangle - \langle B_\infty(x_0, y_0) \rangle)^2 r_m dr_m}, \quad (7)
 \end{aligned}$$

230 with index pairs  $(n, m) = (1, 5), (2, 6), (3, 7)$  and  $(4, 8)$  is used to solve for  $R_n$ . Finally, the boundaries of the target window, are defined by linear interpolation along a circular arc (Fig. 5f). Note that the target window boundaries are largest in the direction approximately parallel to the contours of constant  $\langle B_\infty \rangle$  in Fig. 5a.

Tuning the RMS tolerance, Eq. (7), is discussed in the Supplementary Material. Briefly, the chosen  
 235 value (RMS=1 dB km<sup>-1</sup>), is a balance between being large enough to ensure that there is an adequate spread in ice thickness, whilst being sufficiently small to ensure that attenuation rate values are sufficiently close to the central point of the target window. It will be shown later that, in central Greenland, this condition is generally not satisfied because the gradient in ice thickness with distance is too small. The spatial distribution of the target window radius vectors  $R_1, R_2, R_3, R_4$  for RMS=1  
 240 dB km<sup>-1</sup> using GISM temperature field are shown in Fig. 6. All four plots have the general trend that the target window radi are larger in the interior of the ice-sheet corresponding to where the  $\langle B_\infty \rangle$  field is more slowly varying. The dependence of  $R_1, R_2, R_3, R_4$  upon the anisotropy of the  $\langle B_\infty \rangle$  field in Fig. 4 is also evident, with smaller radi approximately parallel to contours of constant  $\langle B_\infty \rangle$  and larger radi approximately perpendicular. This target windowing approach  
 245 is sensitive to the input temperature field and repeat plots for the SICOPOLIS temperature field are shown in the Supplementary Material. Additionally, we note that the approach is sensitive to the horizontal gradient in (depth-averaged) temperature rather than the absolute value and, thus, systematic biases in the model temperature fields are not important.

## 2.6 Radar-inference of attenuation rate

250 The basic method of using the relationship between ice thickness and bed-returned power to infer the radar-attenuation rate and basal reflection coefficient has been employed many times to local regions of ice-sheets (Gades et al., 2000; Winebrenner et al., 2003; MacGregor et al., 2007; Jacobel et al., 2009; Matsuoka et al., 2012b; Fujita et al., 2012). An explanation of how this method works, begins with the radar power equation

$$255 [P^C] = [R] - [L] + [S], \quad (8)$$

where  $[R]$  is the basal reflection coefficient,  $[L]$  is the total (two way) power loss, and  $[S]$  represents all additional gain characteristics of the radar instrumentation (Matsuoka et al., 2010). In our study



$[P^C]$  is the aggregated geometrically corrected power, as defined by Eqs. (2)-(4), whereas in the majority of other studies  $[P^C]$  is the geometrically corrected peak-power of the basal echo. Equation (8) does not include additional loss due to internal scattering, which can occur when the glacial ice has crevasses and is not well stratified (Matsuoka et al., 2010; MacGregor et al., 2007). Expressing the total loss in terms of the depth averaged attenuation rate as,  $[L] = 2 \langle B \rangle h$ , and then considering the variation in Eq. (8) with respect to ice thickness gives

$$\frac{\delta[P^C]}{\delta h} = \frac{\delta[S]}{\delta h} + \frac{\delta[R]}{\delta h} - 2 \langle B \rangle, \quad (9)$$

(Matsuoka et al., 2010). If both  $\frac{\delta[S]}{\delta h} \ll \frac{\delta[P^C]}{\delta h}$  and  $\frac{\delta[R]}{\delta h} \ll \frac{\delta[P^C]}{\delta h}$ , (refer to Sect. 2.7 for the algorithm quality control measures that test for this), then

$$\langle B \rangle \approx -\frac{1}{2} \frac{\delta[P^C]}{\delta h}. \quad (10)$$

Subsequently, radar-inference of the attenuation rate is achieved via linear regression of Eq. (10), the total loss can be calculated from  $[L] = 2 \langle B \rangle h$ , and the basal reflection coefficients can be calculated from Eq. (8).

As discussed here and in Sect. 2.5, in applying this linear regression approach, it is assumed that the regression gradient (i.e. the depth-averaged attenuation rate) is constant throughout the sample region. In practice, however, the sample region must necessarily include ice with a range of thicknesses, and therefore a range of temperatures and attenuation rates. In our modification to the basic method, the Arrhenius model is used to ‘standardise’ bed-returned power using the central point of each target window as a reference point. This is achieved via the power correction

$$[P^C]_i \rightarrow [P^C]_i + 2(\langle B_\infty(x_i, y_i) \rangle - \langle B_\infty(x_0, y_0) \rangle) h_i, \quad (11)$$

where  $(x_i, y_i)$  corresponds to the position of the  $i$ th data point within the target window and  $(x_0, y_0)$  corresponds to the central point. This power correction represents an estimate of the difference in attenuation loss between an ice column of the actual measurement (loss estimate  $2 \langle B_\infty(x_i, y_i) \rangle h_i$ ), and a fictitious ice column with the same thickness as the measurement but with the attenuation rate of the central point (loss estimate  $2 \langle B_\infty(x_0, y_0) \rangle h_i$ ).

An example of a  $[P^C]$  versus  $h$  regression plot pre- and post- power correction, Eq. (11), is shown in Fig. 7. Typically, ice columns that are thinner/warmer than the central point have  $(\langle B_\infty(x_i, y_i) \rangle - \langle B_\infty(x_0, y_0) \rangle) > 0$  and the power values are increased by Eq. (11), whereas ice columns that are thicker/cooler than the central point have  $(\langle B_\infty(x_i, y_i) \rangle - \langle B_\infty(x_0, y_0) \rangle) < 0$  and the power values are decreased. Subsequently, the power correction acts to enhance the linear correlation between power and ice thickness, (as demonstrated by the increase in the  $r^2$  value in Fig. 7), and enables the underlying attenuation trend to be better discriminated. It follows that, for this typical situation described, failing to take into account the spatial variation in attenuation rate in the linear regression procedure results in a systematic underestimation of the true attenuation rate.



The difference in radar-inferred attenuation rate pre- and post-power correction depends upon the distribution of IPR flight track coverage within the sample region and the size of the sample region defined by Eq. (7), and is typically  $\sim 1\text{-}4 \text{ dB km}^{-1}$ .

295 When applying the linear regression approach described in this section, IPR data from each field season were considered separately. To ensure that there was sufficiently dense data within each sample region a minimum threshold of 20 data measurements was enforced, where each ‘measurement’ corresponds to a separate along-track averaged waveform as described in Sect. 2.3. Additionally, target window centres that were more than 50 km from the nearest IPR data point were excluded.

### 300 2.7 Quality control

When the radar-inferred attenuation rate is obtained via linear regression of  $\frac{\delta[P^C]}{\delta h}$ , Eq. (10), it is assumed that, in comparison, the correlation for  $\frac{\delta[R]}{\delta h}$  is negligible (i.e. that the basal reflector is statistically uniform with ice thickness). To make a prior estimate of the correlation for  $\frac{\delta[R]}{\delta h}$  we use the prior Arrhenius model estimate of the loss and basal reflection coefficient governed by

$$305 [R_\infty] = [L_\infty] + [P^C] + [S] = 2 < B_\infty > h + [P^C] + [S], \quad (12)$$

and consider the correlation and linear regression model for  $\frac{\delta[R_\infty]}{\delta h}$ . The joint quality control threshold:

$$r_{[P^C]}^2 > \alpha, \quad (13)$$

$$r_{ratio}^2 = \frac{r_{[P^C]}^2}{r_{[P^C]}^2 + r_{[R_\infty]}^2} > \beta, \quad (14)$$

310 is then enforced where  $r_{[P^C]}^2$  and  $r_{[R_\infty]}^2$  are  $r^2$  correlation coefficients for the  $\frac{\delta[P^C]}{\delta h}$  and  $\frac{\delta[R_\infty]}{\delta h}$  linear regression models, and  $0 \leq \alpha \leq 1$ ,  $0 \leq \beta \leq 1$  are threshold parameters. This thresholding criteria tests for both strong absolute correlation in  $\frac{\delta[P^C]}{\delta h}$  and strong relative correlation in  $\frac{\delta[P^C]}{\delta h}$  with respect to  $\frac{\delta[R_\infty]}{\delta h}$ . Unlike the use of the Arrhenius model attenuation estimate in Sect. 2.5 and Sect. 2.6, which uses the local difference in the  $< B_\infty >$  field, in Eq. (12) the absolute value of  $< B_\infty >$  is used. A  
 315 justification for the use of the absolute value here, is that it is used only as a quality control measure and does not directly enter the calculation of the radar-inferred attenuation rate.

In general,  $r_{[R_\infty]}^2$  can be high (or equivalently  $r_{ratio}^2$  can be low) due to: (i) there being a true correlation in the basal reflection coefficient with thickness, (ii) there being a correlation due to additional losses other than attenuation such as internal scattering, (iii) the Arrhenius model estimate  
 320 of the attenuation rate being significantly different from the true attenuation rate. Whilst the first two reasons are both desirable for quality control filtering, the third reason is an erroneous effect. However, as the dual threshold filters out all three classes of sample region, this erroneous effect simply reduces the coverage of the algorithm.



## 2.8 Gridded maps

325 The attenuation rate solution from the radar algorithm is at a 1 km grid resolution (set from the scan resolution of the moving target window described in Sect. 2.5). It is defined on the same polar-stereographic coordinate system as in Fig. 1 and the gridded thickness data from Bamber et al. (2013). Subsequently, a gridded data set for the two way loss can be calculated using  $[L] = 2 < B > h$ . For grid cells that contain IPR data, the mean  $[P^C]$  value is calculated, and using Eq. (8) a map  
330 for the gridded relative reflection coefficient,  $[R]$ , is obtained, under the assumption that  $[S]$  is the same for all measurements. Due to the definition of relative power in Eqs. (3) and (4), the values of  $[R]$  are also relative. As described in Sect. 2.3 the averaging procedure for the basal waveforms means that the effective resolution of the processed IPR data varies over the extent of the ice-sheet. Consequently, the number of data points that are averaged in each grid cell varies according to both  
335 this resolution variation and the orientation of the flight tracks relative to the coordinate system. For a single flight line, (i.e. no intersecting flight tracks), the number of points in a grid cell typically ranges from  $\sim 4$  in thick ice to  $\sim 16$  in thin ice.

## 3 Results and discussion

With a view toward identifying regions of the GrIS where the radar algorithm can be applied, we  
340 firstly consider ice-sheet wide properties for the linear regression correlation parameters (Sect. 3.1). We then demonstrate that, on the scale of a major drainage basin, basin 4 in Fig. 1b, the attenuation solution converges for the two input temperature fields (Sect. 3.2). We go on to show that, over this extended region, the converged attenuation solution produces a physically realistic range for the basal reflection coefficients (Sect. 3.3). The relationship between algorithm coverage and uncertainty  
345 is outlined (Sect. 3.4). Finally, we consider how the attenuation solution can be used to predict temperature field bias in thermomechanical ice-sheet models (Sect. 3.5).

### 3.1 Ice-sheet wide properties

Ice-sheet wide maps for the linear regression correlation parameters are shown in Fig. 8a-c using the GISM temperature field as an input. These maps are for the four independently processed field  
350 seasons, and where there are points of coverage overlap an average value is taken. As discussed in Sect. 2.6 and Sect. 2.7, the radar algorithm requires: (i) a strong correlation between bed-returned power and ice thickness (high  $r_{[PC]}^2$ ), (ii) a weak relative correlation between basal reflection and ice thickness (high  $r_{ratio}^2$ ). In general,  $r_{[PC]}^2$  has stronger correlation values in southern Greenland (typical values  $\sim 0.7-0.9$ ). These regions of higher correlation correspond to where there is higher  
355 variation in ice thickness due to basal topography, and are correlated with regions of higher topographic roughness (Rippin, 2013). Correspondingly, in the northern interior of the ice-sheet where the topographic roughness is lower there are weaker correlation values for  $r_{[PC]}^2$  (typically  $\sim 0.2-$



0.3). The correlation values for  $r_{[PC]}^2$  in the northern interior can also, in part, be explained by the lower absolute values for the depth-averaged attenuation rate as predicted in Fig. 4b. The correlation values for  $r_{[R_\infty]}^2$  are generally much lower than  $r_{[PC]}^2$  and more localised. As discussed in Sect. 2.7, regions where  $r_{[R_\infty]}^2$  is high can arise due both true target-window scale variation in the basal reflector or due to a significant bias in the Arrhenius model estimation,  $[R_\infty]$ . The values for  $r_{ratio}^2$  are largely correlated with  $r_{[PC]}^2$ .

Examples of algorithm coverage for three different sets of  $(\alpha, \beta)$  quality control thresholds, Eqs. (13) and (14), are shown in Fig. 8d. These are chosen such that each successively higher quality threshold region is contained within the lower threshold region. In Sect. 3.4 we discuss how the coverage regions relate to uncertainty in the radar-inferred attenuation rate/loss, and the central problem of the radar-inference of the basal material properties. For the discussion here, it is simply important to note that algorithm coverage is fairly continuous for a significant proportion of the southern ice sheet, (corresponding to large regions of major drainage basins 4,5,6,7), and toward the margins of the other drainage basins. The spatial distribution of the radar-inferred attenuation rate,  $\langle B(T_{GISM}) \rangle$  is shown in Fig. 8e and the radar-inferred attenuation loss  $[L(T_{GISM})]$  is shown in Fig. 8f, both for threshold  $(\alpha, \beta) = (0.6, 0.8)$ . Note that the ice-sheet wide properties for  $\langle B(T_{GISM}) \rangle$  are similar to the Arrhenius model predictions (Fig. 4b) with higher values ( $\sim 15\text{-}30 \text{ dB km}^{-1}$ ) toward the ice margins and lower values ( $\sim 7\text{-}10 \text{ dB km}^{-1}$ ) in the interior.

The ice-sheet wide properties of the algorithm are preserved using the SICOPOLIS temperature field as an input (refer to Supplemental Material for a repeat plot of Fig. 8). Notably, the ice-sheet wide distribution for  $r_{[PC]}^2$  is similar, and for equivalent choices of threshold parameters there is better coverage for the southern GrIS than for the northern interior.

### 3.2 Attenuation solution convergence

To demonstrate the convergence of the attenuation solution for different input temperature fields, we compare the solution differences for the (input) Arrhenius models,  $\langle B_\infty(T_{GISM}) \rangle - \langle B_\infty(T_{SIC}) \rangle$  and  $[L_\infty(T_{GISM})] - [L_\infty(T_{SIC})]$ , with the corresponding (output) radar-inferred solution differences,  $\langle B(T_{GISM}) \rangle - \langle B(T_{SIC}) \rangle$  and  $[L(T_{GISM})] - [L(T_{SIC})]$ . As  $[L] = 2 \langle B \rangle h$ , it is necessary to consider the thickness dependence of the solution differences and the consequences for a thickness correlated bias in basal reflection values. We focus on the southeast GrIS, corresponding to target window centres that are located in drainage basin 4 in Fig. 1a. This region is selected post ice-sheet wide processing, and the IPR data from neighboring drainage basins are incorporated in the linear regression plots for the target windows that lie close to the basin boundaries. We consider an attenuation rate solution for fixed threshold parameters  $(\alpha, \beta) = (0.6, 0.8)$ . These are chosen to achieve a solution uncertainty deemed to approach the accuracy required to discriminate basal melt (discussed fully in Sect. 3.4).



The prior Arrhenius model solution difference for the attenuation rate,  $\langle B_{\infty}(T_{\text{GISM}}) \rangle - \langle B_{\infty}(T_{\text{SIC}}) \rangle$ , is strongly negatively biased (Fig. 9a). If the solution difference is aggregated over all grid cells that contain IPR data the mean and standard deviation,  $\mu \pm \sigma$ , is  $-2.42 \pm 0.88 \text{ dB km}^{-1}$  (Fig. 9c). Note, that  $\sigma$  does not represent an uncertainty for the Arrhenius modeled attenuation rate. It is a measure of the spread of the two different input attenuation rate fields. On the scale of the drainage basin, this solution bias is approximately constant with ice thickness (Fig. 9d). By contrast, the radar algorithm solution difference,  $\langle B_{\infty}(T_{\text{GISM}}) \rangle - \langle B_{\infty}(T_{\text{SIC}}) \rangle$ , fluctuates locally between regions of both small positive and negative bias (Fig. 9b). The aggregated radar solution bias is approximately normally distributed about zero,  $\mu \pm \sigma = -0.18 \pm 1.53 \text{ dB km}^{-1}$  (Fig. 9c), and approximately constant with ice thickness (Fig. 9d).

Corresponding difference distributions for the attenuation loss are shown in Fig. 9e and Fig. 9f. These represent a rescaling of the distributions in Fig. 9c and Fig. 9d, by the factor  $2h$  and do not take thickness uncertainty into account. The Arrhenius model solution difference is weakly negatively correlated with thickness ( $r^2=0.09$ ), and from Eq. (8) results in a thickness correlated bias for the basal reflection coefficient. As the attenuation loss solution bias can be  $> 10 \text{ dB}$  for thick ice ( $h \sim 2000 \text{ m}$  or greater), this would potentially result in a different diagnosis of wet and dry glacier beds using the different temperature fields in the Arrhenius model. Again, the radar-inferred solution difference is approximately normally distributed about zero ( $\mu \pm \sigma = -0.56 \pm 5.19 \text{ dB}$ ). The radar-inferred difference is also uncorrelated with ice thickness ( $r^2=0.00$ ) which is essential for unambiguous radar-inference of basal material properties on an ice-sheet wide scale.

If a similar analysis for the attenuation solution differences is applied to drainage basins 3,5,6 we observe algorithm solution convergence, (in the sense of a normally distributed difference centred on zero), and an associated reduction in the solution bias from the Arrhenius model input. In drainage basins 1,2,7,8 we do not observe analogous solution convergence for the radar-inferred values. We do, however, typically see a reduction in the mean systematic bias for the attenuation rate/loss solution relative to the Arrhenius model input. In the Supplementary Material we provide additional plots and discuss the potential reasons for the algorithm non-convergence, which are thought to relate primarily to the more pronounced temperature sensitivity of the algorithm target windows in the northern GrIS.

### 3.3 Attenuation rate and basal reflection maps for the southeast GrIS

For regions of the GrIS where the attenuation rate solution converges and there is algorithm coverage overlap for the different temperature field inputs, it is possible to define the mean radar-inferred attenuation rate solution

$$\langle B \rangle = \frac{1}{2} (\langle B(T_{\text{SIC}}) \rangle + \langle B(T_{\text{GISM}}) \rangle). \quad (15)$$



Note, that the explicit temperature dependence for the mean value is dropped as, for the regions of convergence, it represents a solution that is (approximately) independent of the input temperature field. Within the drainage basins where the solution converges and where only one of  $\langle B(T_{\text{SIC}}) \rangle$  or  $\langle B(T_{\text{GISM}}) \rangle$  is above the coverage threshold, we use the single values to define the mean  $\langle B \rangle$  field. A justification for this approach is that regions where only one temperature field has coverage are most likely an instance of where the other temperature field has erroneous estimates for  $\frac{\delta[R_{\infty}]}{\delta h}$  as discussed in Sect. 2.7. Hence, for a given  $(\alpha, \beta)$  threshold, the coverage region for  $\langle B \rangle$  is slightly larger than for  $\langle B(T_{\text{SIC}}) \rangle$  and  $\langle B(T_{\text{GISM}}) \rangle$ . A regional map for the southeast GrIS using Eq. (15) is shown in Fig. 10. This field is generally smoothly varying, as would be expected given its primary dependence upon temperature.

A gridded map for the basal reflection coefficient along the IPR flight tracks for a 200 km<sup>2</sup> region of the ice sheet is shown in Fig. 11a. This map was produced using the attenuation rate values in Fig. 10 and following the procedure described in Sect. 2.8. The frequency distribution for the relative basal reflection coefficient,  $[R]$ , over the whole drainage basin is shown in Fig. 11b. This distribution corresponds to 63 % of the grid cells that contain IPR data satisfying the waveform processing quality control (Sect. 2.3). The decibel range for the basal reflection coefficient is  $\sim 20$  dB which is consistent with the predicted decibel range for sub-glacial materials (Bogorodsky et al., 1983a), and our estimate of the two-way loss uncertainty ( $\sim 5$  dB), discussed in more detail in Sect. 3.4. The corresponding thickness envelope for the basal reflection coefficients is shown in Fig. 11c.

### 3.4 Relationship between uncertainty and coverage

There are two metrics, both as a function of the quality threshold parameters  $(\alpha, \beta)$ , that we propose can be used to quantify the uncertainty of the radar algorithm. The first metric is the standard deviation of the attenuation solution differences for different input temperature fields as previously described in Sect. 3.2. This metric assesses solution variation due to the target windowing and the local correction to the power within the target window described in Sect. 2.5 and Sect. 2.6 respectively. The second metric is to consider the standard deviation of the attenuation solution differences for independently analysed field seasons for a fixed input temperature field. This metric provides a test that the waveform-processing and system performance is consistent between different field seasons. Furthermore, it provides a test if different flight track distributions and densities in the same target window, produce a similar radar-inferred attenuation rate.

Attenuation rate and loss solution difference distributions for three  $(\alpha, \beta)$  coverage thresholds for the different temperature field inputs (the first uncertainty metric) are shown in Fig. 12a and Fig. 12b respectively, along with corresponding coverage regions in Fig. 12c. As in Sect. 3.2, these distributions are for grid cells that contain IPR data within drainage basin 4. It is clear that the standard deviation of the difference distribution is related to how strict the coverage threshold is, with the strictest coverage threshold having the smallest standard deviation value (refer to plots for



values). Subsequently, we suggest that the coverage of the algorithm is a trade-off with uncertainty. The systematic bias for the strictest coverage threshold,  $(\alpha, \beta) = (0.80, 0.90)$ , is thought to arise due  
465 to sampling an insufficiently small region of the ice-sheet. The standard deviation values in Fig. 12 for drainage basin 4 are similar in the other drainage basins where there is solution convergence. For example, for  $(\alpha, \beta) = (0.60, 0.80)$ ,  $\sigma \sim 1.5 \text{ dB km}^{-1}$  for the attenuation rate difference distribution.

A similar relationship between the choice of  $(\alpha, \beta)$  threshold parameters, and solution accuracy arises for independently analysed field campaign data and a full data table is supplied in the Sup-  
470 plementary Material. The attenuation solution differences distributions are close to being normally distributed about zero, with small systematic biases ( $\sim 0.1\text{-}0.7 \text{ dB km}^{-1}$ ) for the attenuation rate. For the same choice of  $(\alpha, \beta)$  threshold parameters, the attenuation rate solution standard deviations are of similar order to the equivalent temperature field difference distributions. For example, for  $(\alpha, \beta) = (0.60, 0.80)$ ,  $\sigma$  is in the range  $0.98\text{-}1.71 \text{ dB km}^{-1}$  for the different field season pairs.

475 Since for both uncertainty metrics, the solution differences are a function of  $(\alpha, \beta)$ , we suggest that the coverage region can be ‘tuned’ to a desired accuracy. For the problem of basal melt discrimination, where the reflection coefficient difference between water and frozen bedrock is  $\sim 10\text{-}15 \text{ dB}$  (Bogorodsky et al., 1983b), we suggest that standard deviation values for the attenuation loss of  $\sim 5 \text{ dB}$  approach the required accuracy. For both uncertainty metrics this corresponds to approxi-  
480 mately  $(\alpha, \beta) = (0.6, 0.8)$ . This interpretation of uncertainty is consistent with the  $\sim 20 \text{ dB}$  decibel range for the basal reflection coefficients in Fig. 11. Throughout the algorithm development, we continually considered both uncertainty metrics. Of particular note, if the Arrhenius model is used to constrain the target window dimensions (Sect. 2.5), but not to make a power correction within each target window (Sect. 2.6), there are more pronounced systematic biases present for both uncertainty  
485 metrics.

The recent study by Macgregor et al. (2015b) also produced a GrIS wide map for the radar-inferred attenuation rate. This study used returned power from internal layers in the glacier ice to infer the attenuation rate, and the values are therefore only for some fraction of the ice column (roughly corresponding to the isothermal region of the vertical temperature profiles). The uncertainty was  
490 quantified using the attenuation rate solution standard deviation ( $\sigma = 3.2 \text{ dB km}^{-1}$ ) at flight transect crossovers. A direct comparison between their uncertainty estimate and ours is not possible, as we use a different definition of cross-over point (i.e. all grid-cells that contain IPR data in a mutual coverage region), and we can tune the coverage of our algorithm for a desired solution accuracy. Additionally, whereas each value using the internal layer method is spatially independent, the mov-  
495 ing target-windowing approach of our algorithm means each radar-inferred value is dependent upon neighboring estimates.



### 3.5 Prediction of temperature bias of ice-sheet models

The possibility of inverting the Arrhenius relationship, Eq. (A2), to solve for depth-averaged temperature (for an input depth-averaged attenuation rate field) was recently considered by Macgregor et al. (2015b). Radar-inferred temperature values are desirable since they provide a spatially-extensive, independent test of the temperature field produced by thermomechanical ice-sheet models, and for the accuracy of the Arrhenius model parameters to be established. As was proposed by Macgregor et al. (2015b), the inversion of the Arrhenius relationship should ideally take into account layer stratigraphy and spatial variability in the concentration of  $H^+$ ,  $Cl^-$ , and  $NH_4^+$ . However, even for uniform depth-averaged ionic concentrations as described in Sect. 2.4, the relationship between the depth-averaged temperature and the depth-averaged attenuation rate is non-unique. Subsequently, solutions to the inverse problem will depend upon the choice of input temperature profile, and developing a robust inversion procedure requires further investigation.

Here, we estimate temperature field bias using the Arrhenius model-radar algorithm solution differences for the depth-averaged attenuation rate (i.e.  $\langle B_\infty(T_{GISM}) \rangle - \langle B \rangle$  and  $\langle B_\infty(T_{SIC}) \rangle - \langle B \rangle$ ). As discussed above, these solution differences can only give a broad indication regarding the horizontal distribution of depth-averaged temperature bias, and may not hold exactly if ionic concentrations or the shape of the vertical temperature profiles differ substantially over the region. As  $\langle B_\infty(T_{GISM}) \rangle - \langle B \rangle$  is negative over the majority of the southeast GrIS it is suggestive that the depth-averaged GISM temperature field has an overall negative temperature bias in this region (Fig. 13a). Contrastingly, as  $\langle B_\infty(T_{SIC}) \rangle - \langle B \rangle$  is positive over the majority of the same area it is suggestive that the depth-averaged SICOPOLIS temperature field has an overall positive temperature bias in this region (Fig. 13b). Both of these predicted temperature field biases are in agreement with the known model temperature biases at Dye 3 (Fig. 13c). It is also possible to use the ice core temperature profile at Dye 3 in the Arrhenius model to predict a depth-averaged attenuation rate value. This gives  $\langle B_\infty(T_{CORE}) \rangle = 13.9 \text{ dB km}^{-1}$ , which compares with the radar-inferred value of  $\langle B \rangle = 15.8 \text{ dB km}^{-1}$ . These values are consistent within the uncertainty of the Arrhenius model parameters ( $\sim 5 \text{ dB km}^{-1}$  when the temperature field is known (MacGregor et al., 2007)).

## 4 Conclusions

In this study, we considered the first application of a ‘bed-returned power’ radar algorithm for englacial attenuation and basal reflection over the extent of an ice-sheet. In developing our automated, ice-sheet wide, approach we made various refinements to previous regional versions of the algorithm (Gades et al., 2000; MacGregor et al., 2007; Jacobel et al., 2009; Fujita et al., 2012; Matsuoka et al., 2012b). These included using a waveform processing procedure that is specifically tuned for evaluation of bulk material properties, incorporating a prior Arrhenius model estimate for the spatial variation in attenuation to constrain the sample area, standardising the power within



each sample area, and introducing an automated quality control approach based upon the underlying radar equation. We demonstrated regions of attenuation solution convergence for two different input temperature fields and for independently analysed field seasons. A feature of the algorithm is that the uncertainty, as measured by standard deviation of the attenuation solution difference distribution for different input temperature fields and separate field seasons, is tunable. Subsequently, we suggested that the algorithm could be used for the discrimination of bulk material properties over selected regions of ice-sheets. Notably, assuming a total loss uncertainty of  $\sim 5$  dB to be approximately sufficient for basal melt discrimination, we demonstrated that, on the scale of a major drainage basin, the attenuation solution produces a physically realistic ( $\sim 20$  dB) range for the basal reflection coefficient.

We suggest that the converged radar algorithm attenuation solution is preferable to using a forward Arrhenius temperature model to calculate basal reflection coefficients. This is due to the large reduction in the spatially correlated attenuation rate/loss bias that is present in Arrhenius models. With this in mind, the potential problems with using a forward Arrhenius model for bed reflection values were illustrated. Notably, we demonstrated that even a small constant bias in the attenuation rate across a region; (this could be either with respect to a 'true' value or another modelled value), leads to a thickness correlated bias in attenuation loss and therefore the basal reflection coefficients. We hypothesise that the algorithm convergence for different input temperature fields occurs because the local differences in the Arrhenius model attenuation rate field that are used as an algorithm input (i.e.  $\langle B_{\infty}(x, y) \rangle - \langle B_{\infty}(x_0, y_0) \rangle$ ) are more robust than the absolute values. This is broadly equivalent to saying that the horizontal gradients in the depth-averaged temperature field of the ice-sheet models are more robust than the absolute values of the depth-averaged temperature.

In future work, we aim to combine IPR data from preceding CReSIS field campaigns to produce a final gridded data product for the attenuation rate, loss, basal reflection values and basal melt. We have yet to consider an explicit classification of the sub-glacial materials, and quantification of regions of basal melting. It is anticipated that, as outlined by Oswald and Gogineni (2008, 2012); Schroeder et al. (2013), the specular properties of the basal waveform, and how this relates to basal melt detection, could also be incorporated in this analysis. As the regions of algorithm coverage are sensitive to uncertainty, we suggest that these data products could have spatially varying uncertainty incorporated. Additionally, for the basal reflection and basal melt data sets, uncertainty in the measurements of  $[P^C]$  will have to be incorporated in the uncertainty estimate for  $[R]$ . Establishing a procedure for the interpolation of these data sets where either: (i) the algorithm coverage is poor due to low attenuation solution accuracy, or (ii) the IPR data are sparse, will form part of this framework. Regions of lower solution accuracy, generally correspond to the interior of the ice-sheet where spatial variation in the attenuation rate is much less pronounced (primarily the northern interior). Due to this lower spatial variability, (and despite the caveats in the paragraph above), these regions could



potentially have their basal reflection values derived by using forward Arrhenius temperature model for the attenuation.

570 Finally, we envisage that the framework introduced in this paper could be used for radar-inference of radar-attenuation, basal reflection and basal melt for the Antarctic Ice-Sheet. Given that for high solution accuracy the radar algorithm requires high topographic roughness we suggest that IPR data in rougher regions should be analysed first (refer to Siegert et al. (2005) for an overview of East Antarctica). Additionally, the prediction of the temperature field bias using the attenuation rate so-  
 575 lution could be extended to other regions of both the Greenland and Antarctic ice-sheets.

#### Appendix A: Equations for Arrhenius temperature model

In ice, a low loss dielectric, the radar attenuation rate,  $B_\infty$  (in dB km<sup>-1</sup>) is linearly proportional to the high frequency limit of the electrical conductivity,  $\sigma_\infty$  (in  $\mu\text{S m}^{-1}$ ), following the relationship

$$B_\infty = \frac{10 \log_{10} e}{1000 \epsilon_0 c \sqrt{\epsilon_{ice}}} \sigma_\infty, \quad (\text{A1})$$

580 where  $c$  is the vacuum speed of the radio wave (Winebrenner et al., 2003; MacGregor et al., 2007). For  $\epsilon_{ice} = 3.15$ , as is assumed here,  $B_\infty = 0.921 \sigma_\infty$ . The Arrhenius relationship describes the temperature dependence of  $\sigma_\infty$  for ice with ionic impurities present, and is given by

$$\begin{aligned} \sigma_\infty = & \sigma_{pure} \exp \left\{ \frac{E_{pure}}{k_B} \left( \frac{1}{T_r} - \frac{1}{T} \right) \right\} \\ & + \mu_{H^+} c_{H^+} \exp \left\{ \frac{E_{H^+}}{k_B} \left( \frac{1}{T_r} - \frac{1}{T} \right) \right\} \\ & + \mu_{Cl^-} c_{Cl^-} \exp \left\{ \frac{E_{Cl^-}}{k_B} \left( \frac{1}{T_r} - \frac{1}{T} \right) \right\} \\ & + \mu_{NH_4^+} c_{NH_4^+} \exp \left\{ \frac{E_{NH_4^+}}{k_B} \left( \frac{1}{T_r} - \frac{1}{T} \right) \right\}, \end{aligned} \quad (\text{A2})$$

where  $T$  (in K) is the temperature,  $k_B = 1.38 \times 10^{-23} \text{ J K}^{-1}$  is the Boltzmann constant, and  $c_{H^+}$ ,  
 585  $c_{Cl^-}$  and  $c_{NH_4^+}$  are the molar concentrations of the chemical impurities (in  $\mu\text{M}$ ) (MacGregor et al., 2007; Macgregor et al., 2015b). The reference temperature used in the M07 model is  $T_r = 251 \text{ K}$ , which corresponds to activation energies:  $E_{pure} = 0.51 \text{ eV}$ ,  $E_{H^+} = 0.20 \text{ eV}$ ,  $E_{Cl^-} = 0.19 \text{ eV}$ ,  $E_{NH_4^+} = 0.23 \text{ eV}$  (1 eV = 96.5 kJ mol<sup>-1</sup>); electrical conductivity for pure ice  $\sigma_{pure} = 9.2 \mu\text{S m}^{-1}$ ; and molar electrical conductivities:  $\mu_{H^+} = 3.2 \text{ S m}^{-1} \text{ mol}^{-1}$ ,  $\mu_{Cl^-} = 0.43 \text{ S m}^{-1} \text{ mol}^{-1}$ ,  $\mu_{NH_4^+} = 0.19 \text{ S m}^{-1} \text{ mol}^{-1}$   
 590 (MacGregor et al., 2007; Macgregor et al., 2015b). The higher activation energy of pure ice relative to the ionic species explains the greater non-linearity of the pure ice component of  $B_\infty$  in Fig.4a. Following the assumptions in Sect. 2.4 for the GrIS temperature field, ionic concentrations, and ice thickness data set, it is possible to obtain the spatial dependence of the attenuation rate,  $B_\infty(x, y, z)$ , where  $(x, y)$  are planar coordinates and  $z$  is the vertical coordinate. The total (two way) attenuation



595 loss for a vertical column of ice,  $[L_\infty(x, y)]$  (in dB), is then obtained via the depth integral

$$[L_\infty] = 2 \int_0^h B_\infty(z) dz. \quad (\text{A3})$$

Finally, the depth averaged (one-way) attenuation rate,  $\langle B_\infty(x, y) \rangle$  (in dB km<sup>-1</sup>) is calculated from

$$\langle B_\infty \rangle = [L_\infty]/2h. \quad (\text{A4})$$

600 *Acknowledgements.* This study was supported by UK NERC grant NE/M000869/1. The authors would like to thank J. Macgregor, University of Texas, for supplying ice core temperature profiles.



## References

- Bamber, J. L., Griggs, J. A., Hurkmans, R. T. W. L., Dowdeswell, J. A., Gogineni, S. P., Howat, I., Mouginot, J., Paden, J., Palmer, S., Rignot, E., and Steinhage, D.: A new bed elevation dataset for Greenland, *The Cryosphere*, 7, 499–510, doi:10.5194/tc-7-499-2013, 2013.
- Berry, M. V.: The Statistical Properties of Echoes Diffracted from Rough Surfaces, *Philosophical Transactions of the Royal Society A: Mathematical, Physical and Engineering Sciences*, 273, 611–654, doi:10.1098/rsta.1973.0019, 1973.
- Bogorodsky, V. R., Bentley, C. R., and Gudmandsen, P. E.: *Radioglaciology*, chap. 6, p. 216, D. Reidel Publishing Company, 1983a.
- Bogorodsky, V. R., Bentley, C. R., and Gudmandsen, P. E.: *Radioglaciology*, chap. 4, p. 48, D. Reidel Publishing Company, 1983b.
- Cornford, S. L., Martin, D. F., Payne, A. J., Ng, E. G., Le Brocq, A. M., Gladstone, R. M., Edwards, T. L., Shannon, S. R., Agosta, C., van den Broeke, M. R., Hellmer, H. H., Krinner, G., Ligtenberg, S. R. M., Timmermann, R., and Vaughan, D. G.: Century-scale simulations of the response of the West Antarctic Ice Sheet to a warming climate, *The Cryosphere*, 9, 1887–1942, doi:10.5194/tcd-9-1887-2015, 2015.
- Corr, H., Moore, J. C., and Nicholls, K. W.: Radar Absorption due to Impurities in Antarctic Ice, *Geophysical Research Letters*, 20, 1071–1074, 1993.
- Fretwell, P., Pritchard, H. D., Vaughan, D. G., Bamber, J. L., Barrand, N. E., Bell, R., Bianchi, C., Bingham, R. G., Blankenship, D. D., Casassa, G., Catania, G., Callens, D., Conway, H., Cook, A. J., Corr, H. F. J., Damaske, D., Damm, V., Ferraccioli, F., Forsberg, R., Fujita, S., Gim, Y., Gogineni, P., Griggs, J. A., Hindmarsh, R. C. A., Holmlund, P., Holt, J. W., Jacobel, R. W., Jenkins, A., Jokat, W., Jordan, T., King, E. C., Kohler, J., Krabill, W., Riger-Kusk, M., Langley, K. A., Leitchenkov, G., Leuschen, C., Luyendyk, B. P., Matsuoka, K., Mouginot, J., Nitsche, F. O., Nogi, Y., Nost, O. A., Popov, S. V., Rignot, E., Rippin, D. M., Rivera, A., Roberts, J., Ross, N., Siegert, M. J., Smith, A. M., Steinhage, D., Studinger, M., Sun, B., Tinto, B. K., Welch, B. C., Wilson, D., Young, D. A., Xiangbin, C., and Zirizzotti, A.: Bedmap2: Improved ice bed, surface and thickness datasets for Antarctica, *The Cryosphere*, 7, 375–393, doi:10.5194/tc-7-375-2013, 2013.
- Fujita, S., Holmlund, P., Matsuoka, K., Enomoto, H., Fukui, K., Nakazawa, F., Sugiyama, S., and Surdyk, S.: Radar diagnosis of the subglacial conditions in Dronning Maud Land, East Antarctica, *The Cryosphere*, 6, 1203–1219, doi:10.5194/tc-6-1203-2012, 2012.
- Gades, A., Raymond, C., Conway, H., and Jacobel, R.: Bed properties of Siple Dome and adjacent ice streams, West Antarctica, inferred from radio-echo sounding measurements, *Journal of Glaciology*, 46, 88–94, doi:10.3189/172756500781833467, 2000.
- Gillet-Chaulet, F., Gagliardini, O., Seddik, H., Nodet, M., Durand, G., Ritz, C., Zwinger, T., Greve, R., and Vaughan, D. G.: Greenland ice sheet contribution to sea-level rise from a new-generation ice-sheet model, *The Cryosphere*, 6, 1561–1576, doi:10.5194/tc-6-1561-2012, 2012.
- Gogineni, S., Yan, J.-B., Paden, J., Leuschen, C., Li, J., Rodriguez-Morales, Braaten, D., Purdon, K., Wang, Z., Liu, W., and Gauch, J.: Bed topography of Jakobshavn Isbrae, Greenland, and Byrd Glacier, Antarctica, *Journal of Glaciology*, 60, 813–833, doi:10.3189/2014JoG14J129, 2014.



- Greve, R.: Application of a polythermal three-dimensional ice sheet model to the Greenland Ice Sheet: Response to steady-state and transient climate scenarios, *Journal of Climate*, 10, 901–918, doi:10.1175/1520-0442(1997)010<0901:AOAPTD>2.0.CO;2, 1997.
- Gundestrup, N. S. and Hansen, L. H.: Bore-hole survey at Dye 3, South Greenland, *Journal of Glaciology*, 30, 283–288, 1984.
- 645 Howat, I. M., Negrete, A., and Smith, B. E.: The Greenland Ice Mapping Project (GIMP) land classification and surface elevation data sets, *The Cryosphere*, 8, 1509–1518, doi:10.5194/tc-8-1509-2014, 2014.
- Huybrechts, P.: Basal temperature conditions of the Greenland ice sheet during the glacial cycles, *Annals of Glaciology*, 23, 877–887, 1996.
- 650 Jacobel, R. W., Welch, B. C., Osterhouse, D., Pettersson, R., and Gregor, J. A. M.: Spatial variation of radar-derived basal conditions on Kamb Ice Stream, West Antarctica, *Annals of Glaciology*, 50, 10–16, 2009.
- Layberry, R. L. and Bamber, J. L.: A new ice thickness and bed data set for the Greenland ice sheet 2. Relationship between dynamics and basal topography, *Journal of Geophysical Research*, 106, 33 781–33 788, 2001.
- 655 MacGregor, J. A., Winebrenner, D. P., Conway, H., Matsuoka, K., Mayewski, P. A., and Clow, G. D.: Modeling englacial radar attenuation at Siple Dome, West Antarctica, using ice chemistry and temperature data, *Journal of Geophysical Research*, 112, F03 008, doi:10.1029/2006JF000717, 2007.
- MacGregor, J. A., Matsuoka, K., Waddington, E. D., Winebrenner, D. P., and Pattyn, F.: Spatial variation of englacial radar attenuation: Modeling approach and application to the Vostok flowline, *Journal of Geophysical Research*, 117, F03 022, doi:10.1029/2011JF002327, 2012.
- 660 Macgregor, J. A., Fahnestock, M. A., Catania, G. A., Paden, J. D., Gogineni, S. P., Young, S. K., Rybarski, S. C., Mabrey, A. N., Wagman, B. M., and Morlighem, M.: Radiostratigraphy and age structure of the Greenland Ice Sheet, pp. 1–30, doi:10.1002/2014JF003215. Received, 2015a.
- Macgregor, J. A., Li, J., Paden, J. D., Catania, G. A., and Clow, G. D.: Radar attenuation and temperature within the Greenland Ice Sheet, *Journal of Geophysical Research: Earth Surface*, 120, 983–1008, doi:10.1002/2014JF003418, 2015b.
- 665 Matsuoka, K.: Pitfalls in radar diagnosis of ice-sheet bed conditions: Lessons from englacial attenuation models, *Geophysical Research Letters*, 38, 1–5, doi:10.1029/2010GL046205, 2011.
- Matsuoka, K., MacGregor, J. A., and Pattyn, F.: Using englacial radar attenuation to better diagnose the sub-glacial environment: A review, *Proceedings of the 13th International Conference on Ground Penetrating Radar, GPR 2010*, doi:10.1109/ICGPR.2010.5550161, 2010.
- 670 Matsuoka, K., MacGregor, J. A., and Pattyn, F.: Predicting radar attenuation within the Antarctic ice sheet, *Earth and Planetary Science Letters*, 359–360, 173–183, doi:10.1016/j.epsl.2012.10.018, 2012a.
- Matsuoka, K., Pattyn, F., Callens, D., and Conway, H.: Radar characterization of the basal interface across the grounding zone of an ice-rise promontory in East Antarctica, *Annals of Glaciology*, 53, 29–34, doi:10.3189/2012AoG60A106, 2012b.
- 675 Nowicki, S., Bindschadler, R. A., Abe-Ouchi, A., Aschwanden, A., Bueler, E., Choi, H., Fastook, J., Granzow, G., Greve, R., Gutowski, G., Herzfeld, U., Jackson, C., Johnson, J., Khroulev, C., Larour, E., Levermann, A., Lipscomb, W. H., Martin, M. A., Morlighem, M., Parizek, B. R., Pollard, D., Price, S. F., Ren, D., Rignot, E., Saito, F., Sato, T., Seddik, H., Seroussi, H., Takahashi, K., Walker, R., and Wang, W. L.: Insights into spatial
- 680



- sensitivities of ice mass response to environmental change from the SeaRISE ice sheet modeling project II: Greenland, *Journal of Geophysical Research: Earth Surface*, 118, 1025–1044, doi:10.1002/jgrf.20076, 2013.
- Oswald, G. and Gogineni, S.: Recovery of subglacial water extent from Greenland radar survey data, *Journal of Glaciology*, 54, 94–106, doi:10.3189/002214308784409107, 2008.
- 685 Oswald, G. K. A. and Gogineni, S. P.: Mapping Basal Melt Under the Northern Greenland Ice Sheet, *IEEE Transactions on Geoscience and Remote Sensing*, 50, 585–592, doi:10.1109/TGRS.2011.2162072, 2012.
- Paden, J.: Radar Depth Sounder, Centre for Remote Sensings of Ice Sheets, [http://data.cresis.ku.edu/data/rds/rds\\_readme.pdf](http://data.cresis.ku.edu/data/rds/rds_readme.pdf), [last access: Dec 2015], 2015.
- Peters, M. E.: Analysis techniques for coherent airborne radar sounding: Application to West Antarctic ice streams, *Journal of Geophysical Research*, 110, B06 303, doi:10.1029/2004JB003222, 2005.
- 690 Price, S., Lipscomb, W., Hoffman, M., Hagdorn, M., Rutt, I., Payne, T., and Hebel, F.: CISM 2.0.0 Documentation, Los Alamos National Laboratory, [http://oceans11.lanl.gov/cism/data/cism\\_documentation\\_v2.0.pdf](http://oceans11.lanl.gov/cism/data/cism_documentation_v2.0.pdf), [last access: Nov 2015], 2015.
- Price, S. F., Payne, A. J., Howat, I. M., and Smith, B. E.: Committed sea-level rise for the next century from Greenland ice sheet dynamics during the past decade., *Proceedings of the National Academy of Sciences of the United States of America*, 108, 8978–83, doi:10.1073/pnas.1017313108, 2011.
- Rippin, D. M.: Bed roughness beneath the Greenland ice sheet, *Journal of Glaciology*, 59, 724–732, doi:10.3189/2013JoG12J212, 2013.
- Ritz, C., Edwards, T. L., Durand, G., Payne, A. J., Peyaud, V., and Hindmarsh, R. C. A.: Potential sea-level rise from Antarctic ice-sheet instability constrained by observations, *Nature*, 528, 115–118, doi:10.1038/nature16147, 2015.
- 700 Rodriguez-Morales, F., Gogineni, S., Leuschen, C. J., Paden, J. D., Li, J., Lewis, C. C., Panzer, B., Gomez-Garcia Alvestegui, D., Patel, A., Byers, K., Crowe, R., Player, K., Hale, R. D., Arnold, E. J., Smith, L., Gifford, C. M., Braaten, D., and Panton, C.: Advanced multifrequency radar instrumentation for polar Research, *IEEE Transactions on Geoscience and Remote Sensing*, 52, 2824–2842, doi:10.1109/TGRS.2013.2266415, 2014.
- Schroeder, D. M., Blankenship, D. D., and Young, D. A.: Evidence for a water system transition beneath Thwaites Glacier, West Antarctica., *Proceedings of the National Academy of Sciences of the United States of America*, 110, 12 225–8, doi:10.1073/pnas.1302828110, 2013.
- 710 Schroeder, D. M., Grima, C., and Blankenship, D. D.: Evidence for variable grounding-zone and shear-margin basal conditions across Thwaites Glacier, West Antarctica, *Geophysics*, 81, WA35–WA43, doi:10.1190/geo2015-0122.1, 2016.
- Siegert, M. J., Taylor, J., and Payne, A. J.: Spectral roughness of subglacial topography and implications for former ice-sheet dynamics in East Antarctica, *Global and Planetary Change*, 45, 249–263, doi:10.1016/j.gloplacha.2004.09.008, 2005.
- 715 Stillman, D. E., MacGregor, J. A., and Grimm, R. E.: The role of acids in electrical conduction through ice, *Journal of Geophysical Research: Earth Surface*, 118, 1–16, doi:10.1029/2012JF002603, 2013.
- Winebrenner, D., Smith, B., Catania, G., Conway, H., and Raymond, C.: Radio frequency attenuation beneath Siple dome, West antarctica, from wide angle and profiling radar observations, *Annals of Glaciology*, 37, 720 1–7, 2003.



Zwally, H. J., Mario, B. G., Matthew, A. B., and Saba, J. L.: Antarctic and Greenland Drainage Systems, NASA Cryospheric Data, [http://icesat4.gsfc.nasa.gov/cryo\\_data/ant\\_grn\\_drainage\\_systems.php](http://icesat4.gsfc.nasa.gov/cryo_data/ant_grn_drainage_systems.php), [last access: Nov 2015], 2012.



**Table 1.** List of principle symbols

Symbol	Units	Description	Equation(s)
$[P^C]$	dB	Aggregated and geometrically corrected bed-returned power	(2)-(5)
$h$	km	Thickness of ice column	
$B_\infty$	dB km <sup>-1</sup>	Arrhenius model estimate for attenuation rate	(A1), (A2)
$[L_\infty]$	dB	Arrhenius model estimate for total loss	(A3)
$\langle B_\infty \rangle$	dB km <sup>-1</sup>	Arrhenius model estimate for depth-averaged attenuation rate	(A4)
$[R_\infty]$	dB	Arrhenius model estimate for basal power reflection coefficient	(12)
$R_n$	km	Radius vectors for sample regions with $n=1,2,3,4$	
$RMS(R_n)$	dB km <sup>-1</sup>	Root mean square tolerance measure for sample regions	(7)
$[L]$	dB	Radar-inferred value for total loss	
$\langle B \rangle$	dB km <sup>-1</sup>	Radar-inferred value for depth-averaged attenuation rate	(10)
$[R]$	dB	Radar-inferred value for basal power reflection coefficient	(8)
$r_{[P^C]}^2$		$r^2$ correlation coefficient for $[P^C]$ versus $h$	
$r_{[R_\infty]}^2$		$r^2$ correlation coefficient for $[R_\infty]$ versus $h$	
$r_{ratio}^2$		Ratio of $r_{[P^C]}^2$ to $(r_{[P^C]}^2 + r_{[R_\infty]}^2)$	(13)
$\alpha$		Quality control threshold for $r_{[P^C]}^2$	(13)
$\beta$		Quality control threshold for $r_{ratio}^2$	(14)

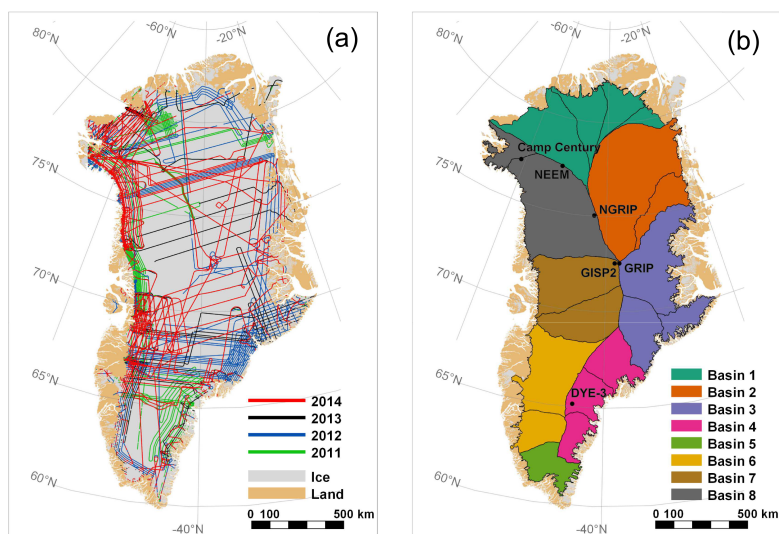


**Figure 1.** (a) Source map for CReSIS flight tracks. (b) Ice core locations and GrIS drainage basins (Zwally et al., 2012). The coordinate system, used throughout this study, is a polar-stereographic projection with reference latitude 71° N and longitude 39° W. The land-ice-sea mask is from Howat et al. (2014).

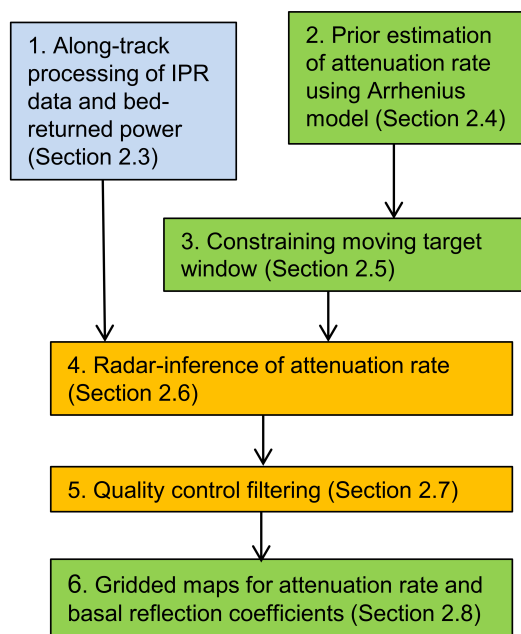


**Figure 2.** Flow diagram for the components of the radar algorithm. The blue box indicates a processing step along a flight track, the green boxes indicate processing steps for a gridded data set of the GrIS, and the orange boxes indicate processing steps for each grid point. IPR data for each field season is considered separately.

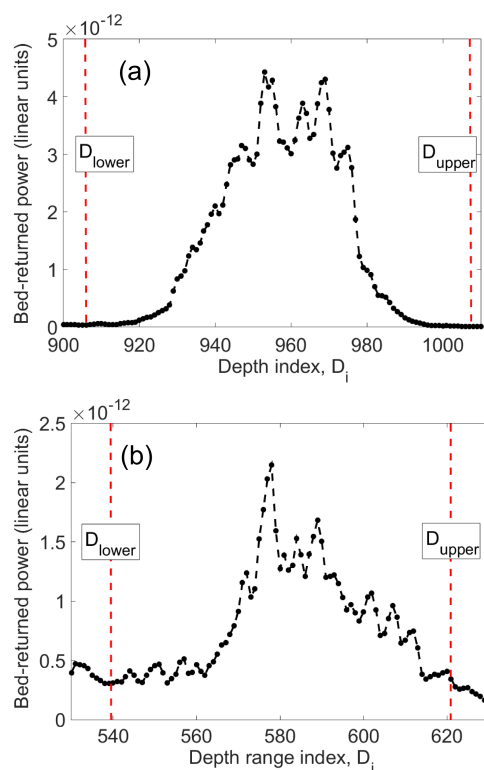
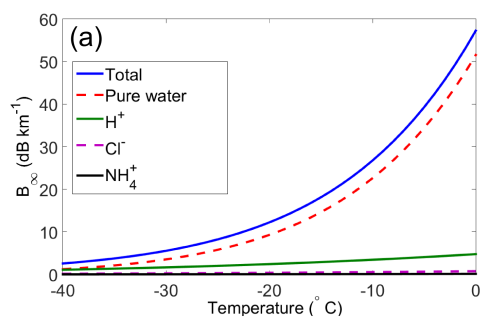
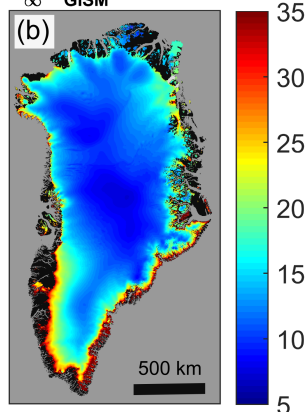


**Figure 3.** Waveform processing using the power depth-integral method, Eq. (2). **(a)** A waveform that satisfies the quality control criteria (decays to 2% of peak power within integral bounds). **(b)** A waveform that does not satisfy the quality control criteria.



$\langle B_{\infty}(T_{\text{GISM}}) \rangle$  (dB km<sup>-1</sup>)



$\langle B_{\infty}(T_{\text{GISM}}) \rangle - \langle B_{\infty}(T_{\text{SIC}}) \rangle$  (dB km<sup>-1</sup>)

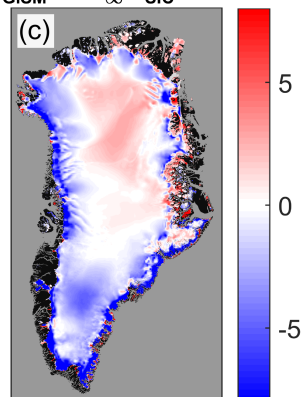


**Figure 4.** Arrhenius model for englacial attenuation. (a) Temperature dependence of attenuation rate,  $B_{\infty}$ , for the M07 model (MacGregor et al., 2007), and depth-averaged ionic concentrations at GRIP core (Macgregor et al., 2015b). (b) Map for the Arrhenius model depth-averaged attenuation rate using the GISM temperature field,  $\langle B_{\infty}(T_{\text{GISM}}) \rangle$ . (c) Depth-averaged attenuation rate difference map for the two temperature fields,  $\langle B_{\infty}(T_{\text{GISM}}) \rangle - \langle B_{\infty}(T_{\text{SIC}}) \rangle$ .

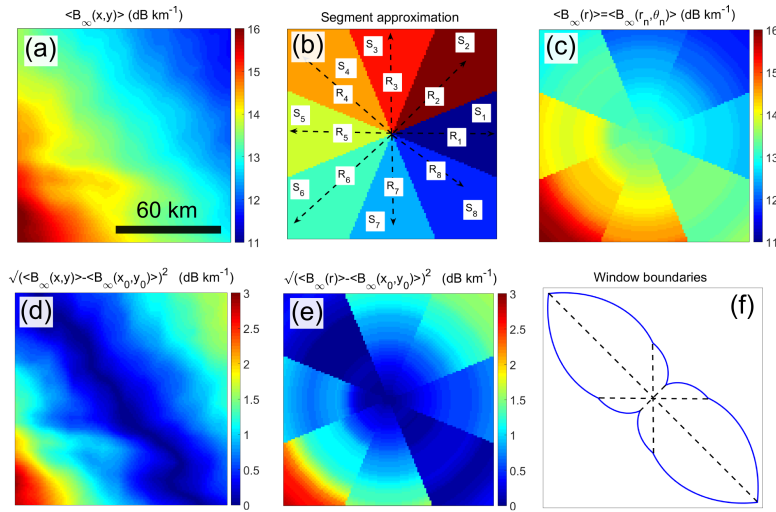


**Figure 5.** Constraining the target window boundaries. (a) Attenuation rate,  $\langle B_\infty(x, y) \rangle$ . (b) Schematic of the segment approximation: segments  $S_n=1, \dots, 7, 8$ , radii  $R_n=1, \dots, 7, 8$  with  $n=1, \dots, 7, 8$ . (c) Segment approximation for the attenuation rate,  $\langle B_\infty(r) \rangle = \langle B_\infty(r_n, \theta_n) \rangle$ , where  $\theta = \frac{(n-1)\pi}{4}$ . (d) The tolerance metric  $\sqrt{\langle B_\infty(x, y) \rangle - \langle B_\infty(x_0, y_0) \rangle}^2$  where  $(x_0, y_0)$  is the central point. (e) Segment approximation for the tolerance metric,  $\sqrt{\langle B_\infty(r) \rangle - \langle B_\infty(x_0, y_0) \rangle}^2$ . (f) Target window boundaries derived from Eq. (7), with RMS= 0.5 dB km<sup>-1</sup>.

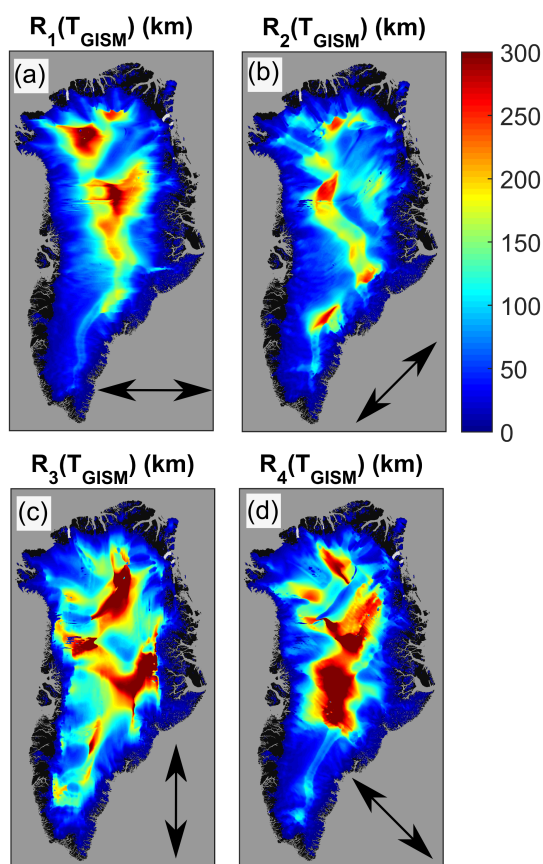


**Figure 6.** Maps for target window radi vectors using the GISM temperature field with  $RMS=1 \text{ dB km}^{-1}$  in Eq. (7). (a)  $R_1$ , (b)  $R_2$ , (c)  $R_3$ , (d)  $R_4$ . The orientation of each radi vector is shown in each subplot.

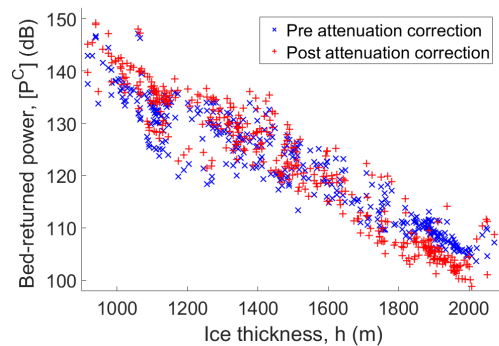


**Figure 7.** Bed-returned power versus ice thickness pre and post attenuation correction, Eq. (11). The radar-inferred attenuation rate pre correction is  $\langle B \rangle = 15.4 \text{ dB km}^{-1}$  ( $r^2 = 0.56$ ) and post correction is  $\langle B \rangle = 19.3 \text{ dB km}^{-1}$  ( $r^2 = 0.89$ ). The central point of the sample region is  $64.30^\circ \text{ N}$ ,  $43.82^\circ \text{ W}$  (100 km due South of the Dye 3 ice core) and has ice thickness 1604 m.

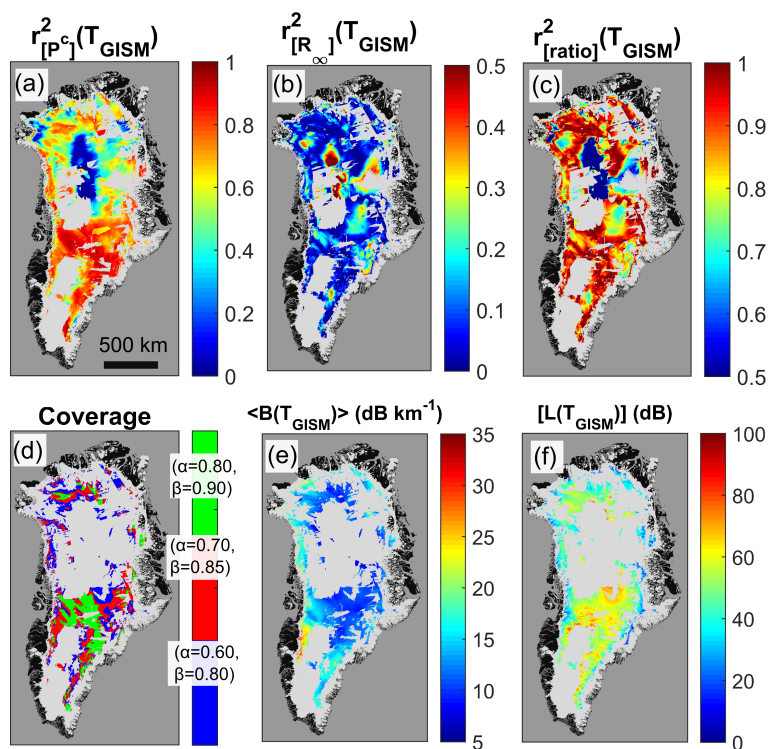


**Figure 8.** Ice-sheet wide properties of the radar algorithm using the GISM temperature field. (a) Power-thickness correlation,  $r_{[P^c]}^2$ . (b) Arrhenius reflection coefficient-thickness correlation,  $r_{[R_\infty]}^2$ . (c) Power ratio-thickness correlation,  $r_{[ratio]}^2$ , Eq. (14). (d) Coverage for three thresholds. (e) Radar-inferred attenuation rate,  $\langle B(T_{GISM}) \rangle$ , for  $(\alpha, \beta) = (0.60, 0.80)$ . (f) Radar-inferred attenuation loss,  $[L(T_{GISM})]$ , for  $(\alpha, \beta) = (0.60, 0.80)$ .

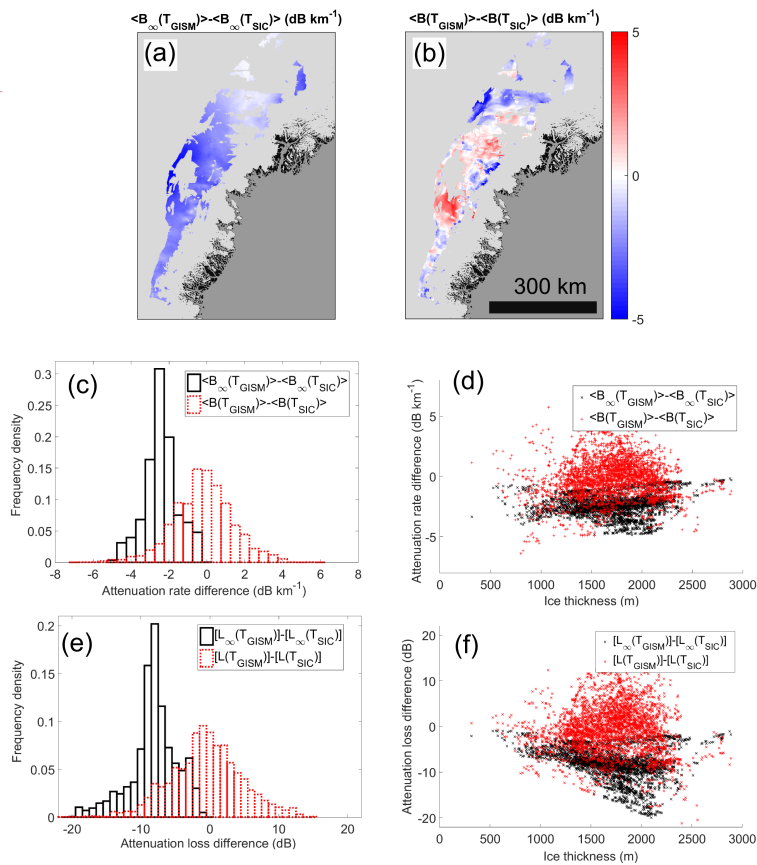


**Figure 9.** Attenuation solution convergence for the SE GrIS. (a) Map for  $\langle B_{\infty}(T_{GISM}) \rangle - \langle B_{\infty}(T_{SIC}) \rangle$  (Arrhenius model input). (b) Map for  $\langle B(T_{GISM}) \rangle - \langle B(T_{SIC}) \rangle$  (algorithm output). (c) Comparison of difference distributions for (a) and (b). (d) Thickness dependence for plot (c). (e) Corresponding difference distributions for attenuation loss. (f) Thickness dependence for plot (e).

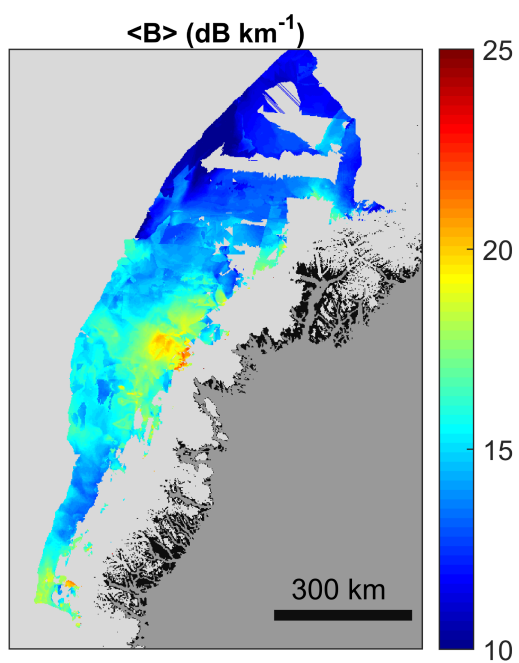
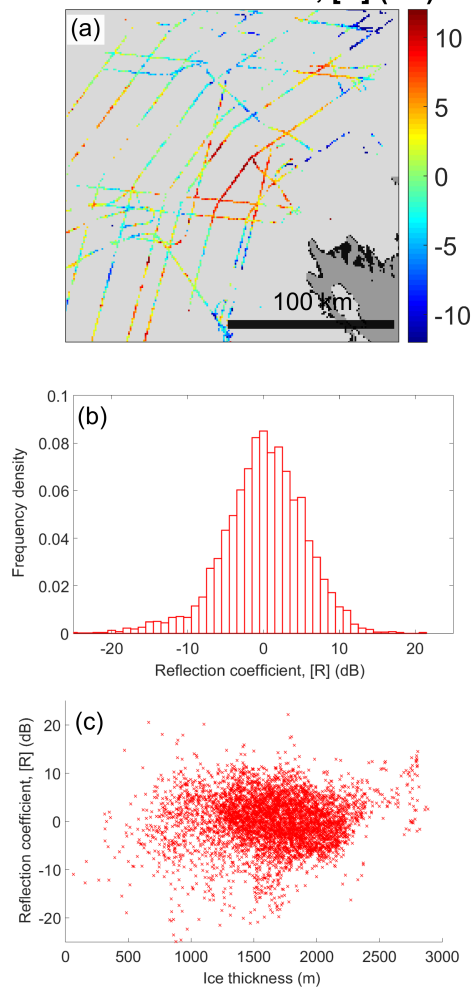


Figure 10. Radar-inferred attenuation rate map for the SE GrIS using Eq. (15).



### Reflection coefficient, [R] (dB)



**Figure 11.** Properties of the basal reflection coefficient for the SE GrIS. (a) An example of a gridded map along the IPR flight tracks. (b) Frequency distribution for drainage basin 4. (c) Thickness dependence for plot (b). The basal reflection coefficients are self-normalised by setting the mean value to be zero.

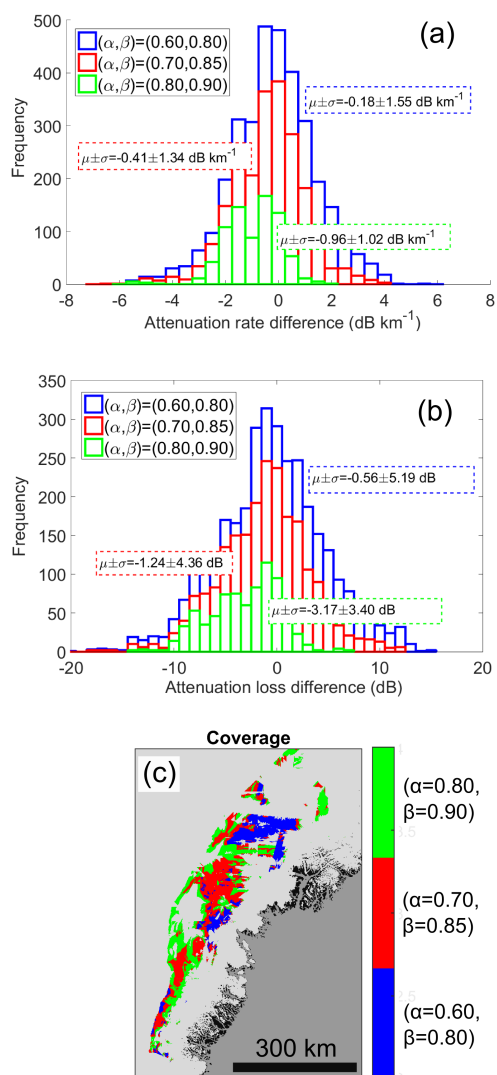


**Figure 12.** Relationship between algorithm coverage and uncertainty as measured by attenuation solution difference distributions. **(a)** Attenuation rate,  $\langle B(T_{\text{GISM}}) \rangle - \langle B(T_{\text{SIC}}) \rangle$ . **(b)** Attenuation loss,  $[L(T_{\text{GISM}})] - [L(T_{\text{SIC}})]$ . **(c)** Algorithm coverage.

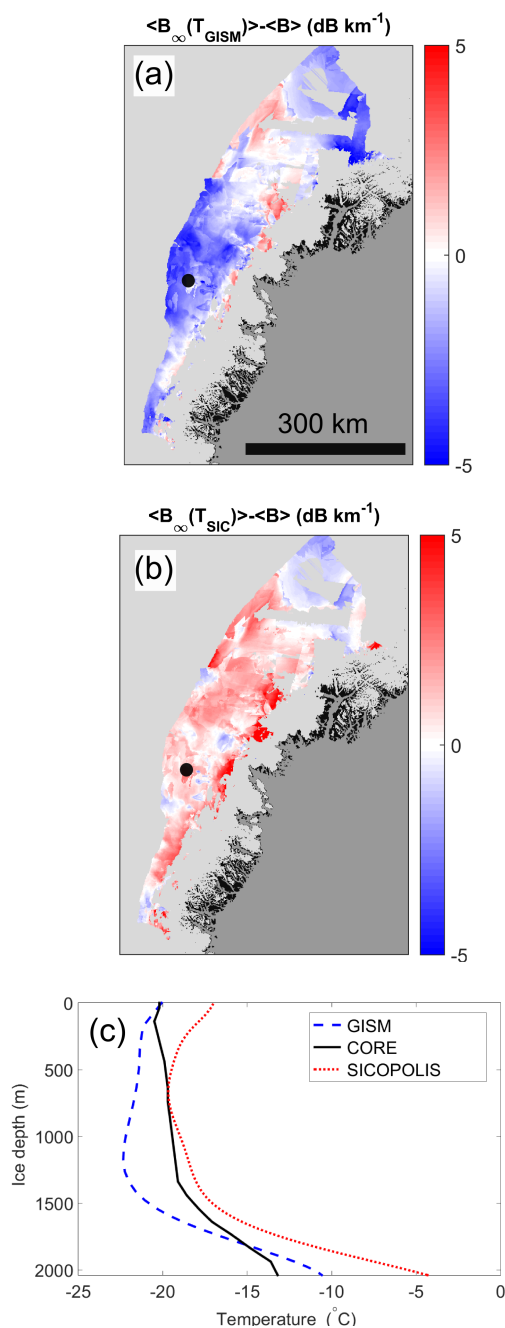


**Figure 13.** Predicted temperature bias for ice-sheet models in the SE GrIS. (a) Map for  $\langle B_{\infty}(T_{\text{GISM}}) \rangle - \langle B \rangle$  (suggestive that depth-averaged GISM temperature field is negatively biased). (b) Map for  $\langle B_{\infty}(T_{\text{SIC}}) \rangle - \langle B \rangle$  (suggestive that depth-averaged SICOPOLIS temperature field is positively biased). (c) Temperature profiles at Dye 3 core (indicated by black circles in (a) and (b)). The core data is from Gundestrup and Hansen (1984).